J. Fluid Mech. (2019), *vol.* 867, *pp.* 1–25.
doi:10.1017/jfm.2019.113

Load and loss for high-speed lubrication flows of pressurized gases between non-concentric cylinders

S. Y. Chien[1],† **and M. S. Cramer**[1]

[1]Engineering Mechanics Program, Virginia Polytechnic Institute and State University, Blacksburg, VA 24060, USA

(Received 17 August 2018; revised 1 November 2018; accepted 2 February 2019; first published online 20 March 2019)

We examine the high-speed flow of pressurized gases between non-concentric cylinders where the inner cylinder rotates at constant speed while the outer cylinder is stationary. The flow is taken to be steady, two-dimensional, compressible, laminar, single phase and governed by a Reynolds lubrication equation. Approximations for the lubricating force and friction loss are derived using a perturbation expansion for large speed numbers. The present theory is valid for general Navier–Stokes fluids at nearly all states corresponding to ideal, dense and supercritical gases. Results of interest include the observation that pressurization gives rise to large increases in the lubricating force and decreases in the fluid friction. The lubrication force is found to scale with the bulk modulus. Within the context of the Reynolds equation an exact relation between total heat transfer and power loss is developed.

Key words: lubrication theory

1. Introduction

Thin viscous films arise in a wide variety of applications including those concerned with rotating machinery, tribology, the spreading of droplets or coatings, particle–particle interaction and bio-lubrication. In such films, inertia is typically ignored and shear forces must be balanced by pressure forces. In lubrication applications, the pressure variations provide the force required to maintain the separation between solid surfaces, i.e. in order to maintain a load. Perhaps the earliest study of such thin film flows was carried out by Reynolds (1886) who stated that the pressure in a steady, incompressible, laminar, two-dimensional thin film satisfies

$$h^3(x)\frac{\mathrm{d}p}{\mathrm{d}x} = 6\mu U h(x) + \text{const.}, \tag{1.1}$$

where $h(x)$ is the film thickness, x is the spatial variable in the main flow direction, $\mu > 0$ is a constant shear viscosity and U is a measure of the relative speed of the solid surfaces being lubricated. Both (1.1) and its first derivative with respect to x are known as the Reynolds equation. In the time since the publication of Reynolds'

† Email address for correspondence: armani23@vt.edu

study, the Reynolds equation has been extended to include the effects of unsteadiness, turbulence, property variations and more complex configurations. In recent years, there has been increasing interest in the use of gases rather than liquids as lubricating fluids; see, e.g. Dostal, Driscoll & Hejzlar (2004), DellaCorte *et al.* (2008), Wright *et al.* (2010), Conboy *et al.* (2012) and Crespi *et al.* (2017). The advantages of gases over liquids are compatibility with working fluids in power systems and turbomachinery, the reduction of weight, the reduction of fouling due to leaks and the reduction of complications due to phase changes. Because the viscosity of gases is smaller than that of high viscosity oils, gas lubrication requires considerably higher speeds than those used in applications involving liquids and the resultant flows are typically taken to be compressible.

Most of the previous investigations of compressible gas lubrication have focused on the behaviour of ideal, i.e. low pressure, gases. Examples include the discussions of Pinkus & Sternlicht (1961), Gross *et al.* (1980), Hamrock, Schmidt & Jacobson (2004), Peng & Khonsari (2004), DellaCorte *et al.* (2008) and Szeri (2010). Recent studies have examined the behaviour of pressurized gases, i.e. gases corresponding to pressures and temperatures of the order of those of the thermodynamic critical point. Studies of lubrication with pressurized gases include those of Conboy (2013), Dousti & Allaire (2016), Kim (2016), Qin (2017), Heshmat, Walton & Cordova (2018) and Guenat & Schiffmann (2018) who applied pure numerical schemes to different versions of the Reynolds equation. The behaviour of pressurized gases in these studies was evaluated using a digital table look-up such as the NIST REFPROP database (Lemmon, Huber & McLinden 2002) used by Conboy (2013), Kim (2016), Qin (2017) and the CoolProp database (Bell *et al.* 2014) used by Guenat & Schiffmann (2018). Dousti & Allaire (2016) have employed a gas model based on a linear pressure–density relation, but this model is not expected to be valid over the full range of pressures and temperatures corresponding to the dense and supercritical regimes (Heshmat *et al.* 2018).

Important differences between pressurized gases and ideal gases are the strong dependence on the thermodynamic state and the rapid and sometimes singular dependence of material properties on the density and temperature. Chien, Cramer & Untaroiu (2017*a*) have examined the approximations leading to the Reynolds equation for compressible flows of pressurized gases. A general form of the Reynolds equation was derived and its range of validity was delineated. In addition to the well-known thin film and lubrication limitations on the film thickness and mild conditions on the imposed temperature difference between isothermal walls, it was shown that the Reynolds equation breaks down in the vicinity of the thermodynamic critical point. It was also shown that the temperature equation can be simplified whenever the Reynolds equation is valid.

In the case of ideal gases governed by the Reynolds equation, the simplest flows are governed by a single parameter referred to as the speed or bearing number (Pinkus & Sternlicht 1961; Gross *et al.* 1980; Hamrock *et al.* 2004; Szeri 2010). The speed number gives a measure of either the flow speed or the overall compressibility of the flow. In the case of pressurized gases, computations must take into account the local thermodynamic state. Chien *et al.* (2017*a*) have shown that the local thermodynamic state enters the problem solely through the effective bulk modulus

$$\kappa_{Te} = \kappa_{Te}(\rho, T) \equiv \frac{\kappa_T(\rho, T)}{\mu(\rho, T)}, \tag{1.2}$$

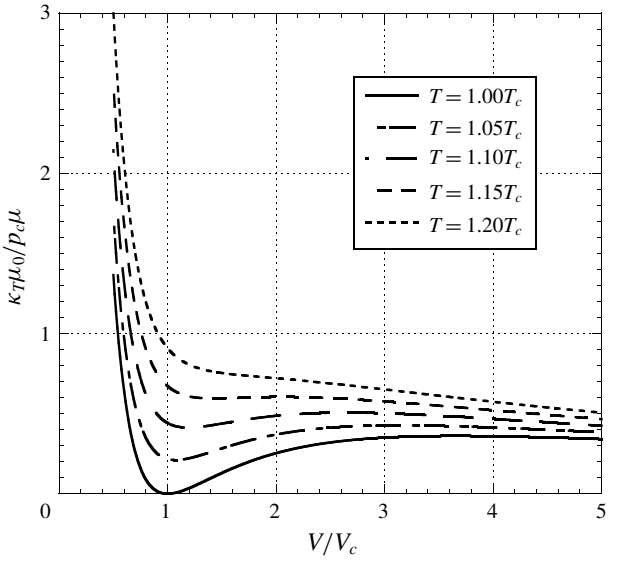

FIGURE 1. Effective bulk modulus of carbon dioxide (CO_2) versus V/V_c. Viscosity model is that of Chung, Lee & Starling (1984), Chung *et al.* (1988) and the gas model is the Redlich–Kwong–Soave (RKS) equation. Here $\mathrm{V} \equiv 1/\rho$ is the specific volume and $\mu_0 = \mu_0(T)$ is the ideal gas ($V \longrightarrow \infty$) value of μ. The subscript 'c' denotes values at the thermodynamic critical point.

where ρ and T are the fluid density and absolute temperature,

$$\kappa_T \equiv \rho \left.\frac{\partial p}{\partial \rho}\right|_T, \tag{1.3}$$

is the bulk modulus of the fluid and $p = p(\rho, T)$ is the thermodynamic pressure. The effective bulk modulus (1.2) is recognized as a measure of the local fluid stiffness to the local shear forces.

In the limit of ideal gases, the effective bulk modulus (1.2) increases monotonically with pressure or density at constant temperatures. In the case of pressurized gases, the variation of κ_{Te} is no longer monotonically increasing with pressure and can take on relatively small values in the general neighbourhood of the thermodynamic critical point. To illustrate this variation we have plotted the variation of a scaled version of (1.2) along isotherms in figure 1.

A non-dimensional measure of the flow speed or the overall compressibility of the flow is the speed or bearing number defined as

$$\Lambda \equiv 6\frac{UL}{h_o^2 \kappa_{Te}|_{ref}}, \tag{1.4}$$

where U, L and h_o are measures of the flow speed, length scale in the general flow direction and the gap width, respectively, and are defined more precisely in the next section. The quantity $\kappa_{Te}|_{ref}$ is the effective bulk modulus (1.2) evaluated at a reference thermodynamic state. The form (1.4) is that given by Chien *et al.* (2017*a*), Chien, Cramer & Untaroiu (2017*b*) and arises naturally when pressurized gases are considered.

In many applications the speed number (1.4) is relatively large partly due to the need to generate sufficiently large lubrication forces and partly to avoid thermal runaway instabilities. Such instabilities will result in excessive heating of the solid components of the device resulting in thermal expansion which in turn can lead to metal-on-metal contact and failure of the bearing; see, e.g. the discussions of Howard *et al.* (2007) and Briggs *et al.* (2008). Gross *et al.* (1980) was one of the first to derive the analytical solutions to the Reynolds equation for lubrication flows with large speed numbers. Peng & Khonsari (2004) adopted a similar approach to evaluate the lowest-order load generated by different configurations. However, the approximate solutions provided by Gross *et al.* (1980) and Peng & Khonsari (2004) are valid for low-pressure gases only and thermal effects were not considered.

Chien & Cramer (2019) have presented approximate solutions to the Reynolds and corresponding temperature equation for the local values of the density, pressure, temperature and heat flux valid for flows of pressurized gases with large speed numbers. These solutions reveal the role played by material functions, e.g. the effective bulk modulus and thermal expansivity, in the variation of the fundamental local quantities. The goal of the present study is to develop approximations for the total force and total friction loss valid for large speed numbers. The results will be valid everywhere the Reynolds equation of Chien *et al.* (2017*a*) is, i.e. at all pressures and temperatures in the ideal, dense and supercritical gas regimes except sufficiently close to the thermodynamic critical point. Although the first-order theory described by Chien & Cramer (2019) is sufficient to find the first corrections to the density, pressure and temperature distributions, we have found that the first corrections to global parameters such as load, loss and net heat transfer require expansions which are second order in Λ^{-1}.

Because our primary interest is to examine the effects of pressurization and finite speed number (1.4), we follow previous investigators in restricting attention to a simple canonical lubrication model, i.e. that of Chien *et al.* (2017*a*), which is the simplest model for compressible thin film flows of high-pressure gases. In addition to requiring the usual thin film conditions of a small lubrication Reynolds number and small layer thickness, Chien *et al.* (2017*a*) have required that the thermodynamic states be sufficiently far from those of the thermodynamic critical point; order of magnitude estimates for the size of the near-critical condition in the context of thin films were given by Chien *et al.* (2017*a*). The particular form of the Reynolds and temperature equation used here is valid for steady, laminar, two-dimensional and single-phase gas flows. Here we focus on supercritical temperatures so that multiphase flows will not be relevant. The motivation for the restriction to two-dimensional steady flows is done in order to focus attention on the new behaviour arising from pressurization. The condition of two-dimensional flow will be approximately satisfied for long bearings near the plane of symmetry. As demonstrated by Szeri (2010), a Reynolds equation for turbulent flows can be developed, but its form is essentially the same as that used here with a Reynolds number dependent turbulent viscosity and other average properties replacing the local values used here.

In order to present concrete results, we examine the simple case of non-concentric cylinders: the details of this configuration are described in the next section. The large speed number approximations are developed in § 3. We compare our approximations to numerical solutions of the compressible Reynolds equation in § 4. A short derivation of the relation between power loss and heat transfer leaving the fluid film is given in appendix A. The latter result is exact within the context of the Reynolds equation.

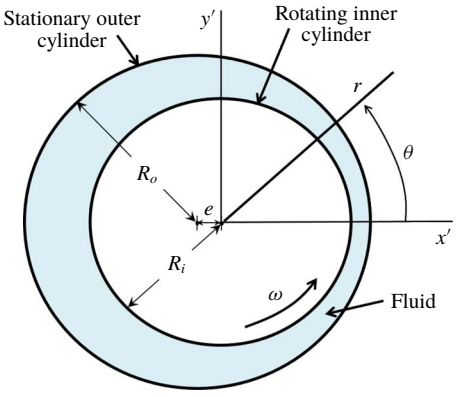

FIGURE 2. (Colour online) Sketch of physical configuration.

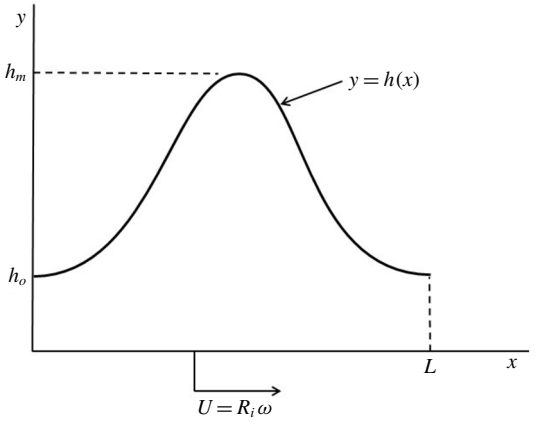

FIGURE 3. Unwrapped configuration. The stationary outer cylinder of figure 2 is approximated by the $y = h(x)$ surface and the rotating inner cylinder is approximated by the $y = 0$ surface. The minimum gap width is $h_o \equiv h(0)$ and the maximum value of $h(x)$ is $h_m \equiv h(L/2)$.

2. Formulation

The physical configuration is that sketched in figure 2. The flow is taken to be contained between the inner and outer cylinders depicted there. The inner cylinder has a radius R_i and the outer cylinder has a radius R_o. The origin of the stationary x'–y' coordinate system is located at the centre of the inner cylinder. The centre of the outer cylinder is located at $x' = -e, y' = 0$. The inner cylinder rotates at a constant rate ω while the outer cylinder is stationary. For convenience, we refer to the inner cylinder as the rotor and the outer cylinder as the stator.

Throughout this work we apply the thin film approximation so that we compute the flow details using the 'unwrapped' configuration sketched in figure 3. When $R_o \approx R_i$ the fluid can be taken to be contained in the region $0 \leqslant y \leqslant h(x)$, where the variable y is recognized as a distance measured normal to the inner cylinder and $x \equiv \theta R_i$ is distance measured along the inner cylinder. The curve $y = h(x)$ in figure 3 approximately corresponds to the surface of the stator. We can now define

$L \equiv 2\pi R_i$ which is just the circumference of the inner cylinder and $h_o \equiv h(0)$ which is the minimum gap width; we take h_o to be a measure of the film thickness. For the non-concentric cylinders sketched in figure 2, the thickness of the fluid layer can be approximated by

$$\overline{h} \equiv \frac{h(x)}{h_o} \approx 1 + \delta - \delta\cos(\theta), \tag{2.1}$$

where

$$\delta \equiv \frac{1}{2}(\overline{h}_m - 1) = \frac{\epsilon}{1-\epsilon}. \tag{2.2}$$

The quantity $\overline{h}_m \equiv \overline{h}(\bar{x} = 1/2) = \overline{h}(\theta = \pi)$ is the maximum value of $\overline{h}$. The factor δ has been related to the eccentricity ratio $\epsilon \equiv e/c$ where $c \equiv R_o - R_i$ is called the radial clearance; the eccentricity ϵ is commonly used in the lubrication literature; see, e.g. Pinkus & Sternlicht (1961), Gross *et al.* (1980), Hamrock *et al.* (2004) or Szeri (2010).

In our detailed calculations we will employ (2.1). However, many of our results are also valid under the weaker condition that $\overline{h}$ be symmetric about $\theta = \pi$, i.e.

$$\overline{h}(\pi - \theta) \equiv \overline{h}(\theta - \pi). \tag{2.3}$$

As a result, the derivatives of $\overline{h}(\theta)$ will satisfy

$$\frac{\mathrm{d}\overline{h}}{\mathrm{d}\theta}(\pi - \theta) = -\frac{\mathrm{d}\overline{h}}{\mathrm{d}\theta}(-(\pi - \theta)). \tag{2.4}$$

In order to ensure that $\overline{h}$ is a minimum at $\bar{x} = 0,\ 1$ or $\theta = 0, 2\pi$, we require that

$$\begin{aligned} \frac{\mathrm{d}\overline{h}}{\mathrm{d}\theta} &\geqslant 0 \text{ if } 0 \leqslant \theta \leqslant \pi \\ &\leqslant 0 \text{ if } \pi \leqslant \theta \leqslant 2\pi. \end{aligned} \tag{2.5}$$

The flow will be taken to be steady, two-dimensional, compressible, single phase and laminar. The physical flow is required to satisfy the usual thin film and lubrication restrictions, i.e.

$$\frac{h_o}{L} \ll 1, \tag{2.6}$$

$$Re\frac{h_o^2}{L^2} \ll 1, \tag{2.7}$$

where Re is the Reynolds number based on L, $U \equiv R_i\omega$, μ_{ref} and ρ_{ref}. The subscript 'ref' will always refer to quantities evaluated at a given reference thermodynamic state. Here we take that reference state to be that at $x = 0$ and L. As discussed by Chien *et al.* (2017*a*) we also need to require that the flow be sufficiently far from the thermodynamic critical point. If the rotor and stator are both isothermal, we must also require that the product of the fixed, known temperature difference and the thermal expansion coefficient defined by (A 6) be small. Under these conditions, the flow will satisfy the Reynolds equation of Chien *et al.* (2017*a*) which can be written in non-dimensional form as

$$\frac{\mathrm{d}}{\mathrm{d}\bar{x}}\left(\overline{h}^3\overline{\kappa}_{Te}\frac{\mathrm{d}\overline{\rho}}{\mathrm{d}\bar{x}}\right) = \Lambda\frac{\mathrm{d}(\overline{\rho}\overline{h})}{\mathrm{d}\bar{x}}, \tag{2.8}$$

where $\overline{\rho} \equiv \rho/\rho_{ref}$ is the non-dimensional density. Here $\overline{x} \equiv x/L$ and

$$\overline{\kappa}_{Te} = \overline{\kappa}_{Te}(\overline{\rho}) \equiv \frac{\kappa_{Te}(\rho, T_{ref})}{\kappa_{Te}|_{ref}} = \frac{\kappa_{Te}(\rho, T_{ref})}{\kappa_{Te}(\rho_{ref}, T_{ref})} \tag{2.9}$$

is the scaled effective bulk modulus. For the present purposes, the Reynolds equation (2.8) will be integrated subject to the periodicity conditions

$$\overline{\rho}(0) = \overline{\rho}(1) = 1. \tag{2.10}$$

The solution for the fluid density is generally obtained by integrating (2.8) subject to (2.10) to yield $\overline{\rho} = \overline{\rho}(\overline{x};\ \Lambda)$ once the reference thermodynamic state (ρ_{ref}, T_{ref}) and gas models are specified. The pressure is then found by substitution in the equation of state.

In the following discussion, a convenient first integral of (2.8) is

$$\overline{\rho} = \frac{1}{\overline{h}} + \frac{1}{\Lambda}\left(\overline{h}^2\overline{\kappa}_{Te}\frac{\mathrm{d}\overline{\rho}}{\mathrm{d}\overline{x}} - \frac{1}{\overline{h}}\frac{\mathrm{d}\overline{\rho}}{\mathrm{d}\overline{x}}(0)\right), \tag{2.11}$$

where we have used the fact that $\overline{h} = \overline{\kappa}_{Te} = 1$ at $\overline{x} = 0$. In the limit of incompressible flow with constant viscosity (2.11) reduces to Reynolds' original formula (1.1) with

$$\frac{\mathrm{d}\overline{\rho}}{\mathrm{d}\overline{x}}(0) \tag{2.12}$$

playing the role of the integration constant.

With the thin film approximation (2.6) we can write the x' and y' components of the forces on the rotor from the fluid as

$$\overline{F}_{x'} \approx \int_0^{2\pi} \overline{p}\cos(\theta)\,\mathrm{d}\theta = -\frac{1}{2\pi}\int_0^{2\pi} \frac{\mathrm{d}\overline{p}}{\mathrm{d}\overline{x}}\sin(\theta)\,\mathrm{d}\theta, \tag{2.13}$$

$$\overline{F}_{y'} \approx \int_0^{2\pi} \overline{p}\sin(\theta)\,\mathrm{d}\theta = \frac{1}{2\pi}\int_0^{2\pi} \frac{\mathrm{d}\overline{p}}{\mathrm{d}\overline{x}}\cos(\theta)\,\mathrm{d}\theta, \tag{2.14}$$

where

$$\overline{\boldsymbol{F}} \equiv -\frac{h_o^2}{\mu_{ref}U2\pi R_i^2 b}\boldsymbol{F}', \tag{2.15}$$

b is the length of the cylinders in the z'-direction, and $\boldsymbol{F}'$ is the dimensional force on the rotor. The quantity $\overline{p}$ is the scaled pressure and is related to the dimensional pressure p by

$$\overline{p} \equiv \frac{h_o^2}{\mu_{ref}UL}(p - p_{ref}). \tag{2.16}$$

The power loss is the work per time done on the rotor, i.e. the $y = 0$ surface in figure 3. In the thin film approximation, this can be written

$$P = bU\int_0^L T_{yx}\,\mathrm{d}x \approx \frac{bLU^2\mu_{ref}}{h_o}\overline{P}, \tag{2.17}$$

where the scaled loss is

$$\overline{P} \equiv \int_0^1 \left(\overline{\mu}\frac{\partial u}{\partial \overline{y}}\right)\bigg|_{\overline{y}=0} \mathrm{d}\overline{x}, \tag{2.18}$$

$\overline{\mu} \equiv \mu/\mu_{ref}$ is a scaled version of the viscosity, and $\overline{y} \equiv y/h_o$ is the scaled y-coordinate. The x-component of the fluid velocity, denoted by u, is scaled with U and its expression is given in appendix A.

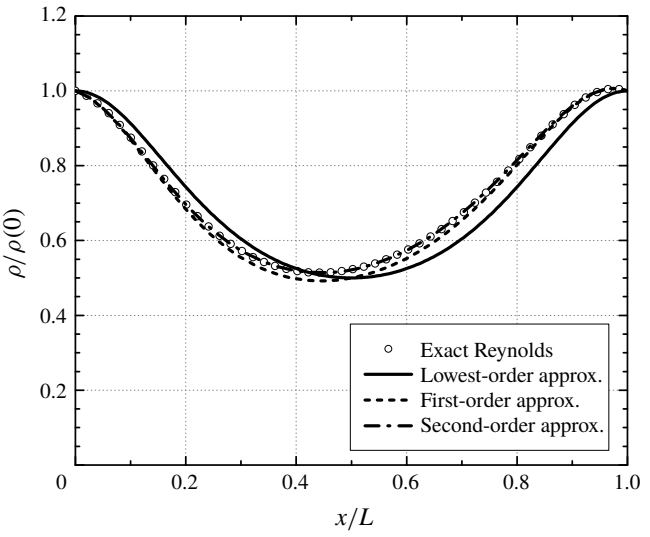

FIGURE 4. Scaled density versus x/L at $V(0) = V(L) = 10V_c$, $T(0) = T(L) = 1.05T_c$, $\delta = 0.5$, $\Lambda = 40$. The symbols ○ denote the exact solutions to the Reynolds equation (2.8). The solid line denotes the lowest-order solutions, i.e. $\overline{\rho} = 1/\overline{h}$. The dashed and dash-dot lines represent the first- and second-order solutions of the scaled density (3.1), respectively.

3. General results

We now determine the approximate solutions to the Reynolds equation (2.8) for lubrication flows with large speed numbers. We first consider the second-order expansion for density, i.e.

$$\overline{\rho} = \rho_0 + \frac{\rho_1}{\Lambda} + \frac{\rho_2}{\Lambda^2} + O\left(\frac{1}{\Lambda^3}\right). \tag{3.1}$$

If we substitute (3.1) and its derivative in (2.11), we then obtain the functions

$$\rho_0 = \frac{1}{\overline{h}}, \tag{3.2}$$

$$\rho_1 = -\overline{\kappa}_{Teo}\frac{\mathrm{d}\overline{h}}{\mathrm{d}\overline{x}}, \tag{3.3}$$

$$\rho_2 = -\overline{h}^2\frac{\mathrm{d}}{\mathrm{d}\overline{x}}\left(\overline{\kappa}_{Te}^2\frac{\mathrm{d}\overline{h}}{\mathrm{d}\overline{x}}\right)\bigg|_o + \frac{1}{\overline{h}}\frac{\mathrm{d}^2\overline{h}}{\mathrm{d}\overline{x}^2}(0), \tag{3.4}$$

where the subscript 'o' will always refer to quantities evaluated at the lowest-order density, $\overline{\rho} \approx 1/\overline{h}$. For example,

$$\overline{\kappa}_{Teo}(\overline{\rho}) \equiv \overline{\kappa}_{Te}\left(\frac{1}{\overline{h}}\right). \tag{3.5}$$

It is easily verified that (3.1)–(3.4) satisfy the boundary conditions (2.10) and the equation for $\overline{h}$, i.e. (2.1), to the appropriate order.

To demonstrate the accuracy of (3.1)–(3.4), we have plotted a comparison of the approximate density (3.1) and the numerical solution to the exact Reynolds equation (2.8) at $\Lambda = 40$ in figures 4–5. Here we take the channel sketched in figure 3 to be

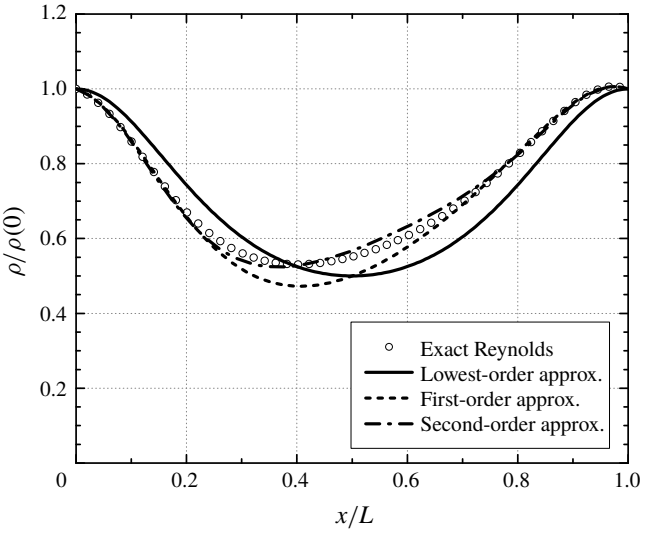

FIGURE 5. Scaled density versus x/L at $V(0) = V(L) = 2V_c$, $T(0) = T(L) = 1.05T_c$, $\delta = 0.5$, $\Lambda = 40$. The symbols ○ denote the exact solutions to the Reynolds equation (2.8). The solid line denotes the lowest-order solutions, i.e. $\overline{\rho} = 1/\overline{h}$. The dashed and dash-dot lines represent the first- and second-order solutions of the scaled density (3.1), respectively.

given by $h_o/L = 1.989 \times 10^{-5}$, and $\delta = 0.5$. The gas models are taken to be those described in § 4. The temperature at the entrance and exit is taken to be $T(0) = T(L) = 1.05T_c$. In figure 4 the specific volume, i.e. $V \equiv 1/\rho$, is taken to satisfy $V(0) = V(L) = 10V_c$. The pressure at this state is approximately 21.2 bar $\approx 0.29p_c$, so that the thermodynamic state can be regarded as that of a dense gas. In figure 5 we consider the case of a slightly supercritical fluid in which the reference specific volume is taken to be $V(0) = V(L) = 2V_c$ and the corresponding pressure is approximately 78.2 bar $\approx 1.06p_c$.

Inspection of figures 4 and 5 reveals that the second-order approximation is in excellent agreement with the exact solutions. As compared to the lowest-order approximation, the first-order term corrects the slope of the curves near both ends of the channel whereas the second-order correction term further improves the prediction of the position and magnitude of the local minimum.

The accuracy of our approximation for both cases increases as $\Lambda \longrightarrow \infty$. In order to illustrate the accuracy of the approximation, we have also plotted the root-mean-square error (RMSE) between the approximate density (3.1) and the exact solution to the Reynolds equation (2.8) as a function of Λ in figure 6. It was found that the second-order approximation can provide reasonable accuracy when $\Lambda \geqslant 20$. When $\Lambda = 20$, the RMSEs of the second-order approximation for cases of $V(0) = V(L) = 10V_c$ and $2V_c$ are approximately 1.4 % and 8 %, respectively.

We now turn to the determination of the large Λ approximation for the forces, i.e. (2.13) and (2.14), on the rotor. If we use (1.3), (1.4) and (2.16), the expressions for the exact force components (2.13) and (2.14) can be rewritten as

$$-\frac{\Lambda}{6}\overline{F}_{x'} = \frac{1}{2\pi}\int_0^{2\pi} \mathscr{R}\frac{\mathrm{d}\overline{\rho}}{\mathrm{d}\overline{x}}\sin(\theta)\,\mathrm{d}\theta, \tag{3.6}$$

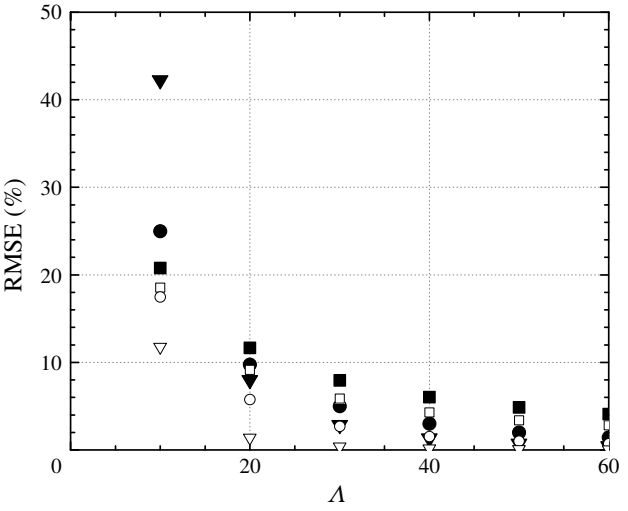

FIGURE 6. Root-mean-square error (RMSE) between the approximate and exact density versus Λ at $T(0) = T(L) = 1.05T_c$ and $\delta = 0.5$. The symbols ■, ● and ▼ represent the lowest-, first- and second-order approximations, respectively, at $V(0) = V(L) = 2V_c$. The symbols □, ○ and ▽ represent the lowest-, first- and second-order approximations, respectively, at $V(0) = V(L) = 10V_c$.

$$\frac{\Lambda}{6}\overline{F}_{y'} = \frac{1}{2\pi}\int_0^{2\pi} \mathscr{R}\frac{\mathrm{d}\overline{\rho}}{\mathrm{d}\overline{x}}\cos(\theta)\,\mathrm{d}\theta, \tag{3.7}$$

where the factor

$$\mathscr{R} = \mathscr{R}(\overline{\rho}, T_{ref}) \equiv \frac{\overline{\kappa}_T}{\overline{\rho}}, \tag{3.8}$$

can be expanded in a Taylor series for $\overline{\rho}$ near $1/\overline{h}$ yielding

$$\mathscr{R}(\overline{\rho}, T_{ref}) = \mathscr{R}_o + \left.\frac{\mathrm{d}\mathscr{R}}{\mathrm{d}\overline{\rho}}\right|_o \left(\overline{\rho} - \frac{1}{\overline{h}}\right) + \frac{1}{2}\left.\frac{\mathrm{d}^2\mathscr{R}}{\mathrm{d}\overline{\rho}^2}\right|_o \left(\overline{\rho} - \frac{1}{\overline{h}}\right)^2 + O\left(\frac{1}{\Lambda^3}\right). \tag{3.9}$$

If we combine (3.9) with (3.1), and multiply the result by the derivative of (3.1), we find

$$\mathscr{R}\frac{\mathrm{d}\overline{\rho}}{\mathrm{d}\overline{x}} = \mathscr{R}_o\frac{\mathrm{d}\rho_0}{\mathrm{d}\overline{x}} + \frac{1}{\Lambda}\frac{\mathrm{d}(\mathscr{R}_o\rho_1)}{\mathrm{d}\overline{x}} + \frac{1}{\Lambda^2}\frac{\mathrm{d}}{\mathrm{d}\overline{x}}\left[\mathscr{R}_o\rho_2 + \frac{1}{2}\left.\frac{\mathrm{d}\mathscr{R}}{\mathrm{d}\overline{\rho}}\right|_o \rho_1^2\right] + O\left(\frac{1}{\Lambda^3}\right). \tag{3.10}$$

Through substitution of (3.2)–(3.4) and (3.10) in (3.6) and straightforward manipulation we then obtain

$$-\frac{\pi\Lambda}{3}\overline{F}_{x'} = I_{x1} + \frac{I_{x2}}{\Lambda} + \frac{I_{x3}}{\Lambda^2} + O\left(\frac{1}{\Lambda^3}\right), \tag{3.11}$$

where the quantities

$$I_{x1} \equiv -2\pi\int_0^{2\pi} \frac{\overline{\kappa}_{To}}{\overline{h}}\frac{\mathrm{d}\overline{h}}{\mathrm{d}\theta}\sin(\theta)\,\mathrm{d}\theta, \tag{3.12}$$

$$I_{x2} \equiv 4\pi^2 \int_0^{2\pi} \overline{\kappa}_{To}\overline{\kappa}_{Teo}\overline{h}\frac{\mathrm{d}\overline{h}}{\mathrm{d}\theta}\cos(\theta)\,\mathrm{d}\theta, \tag{3.13}$$

$$\begin{aligned} I_{x3} \equiv & -8\pi^3 \int_0^{2\pi} \left[\frac{1}{2}\overline{\kappa}_{Teo}^2\frac{\mathrm{d}}{\mathrm{d}\overline{\rho}}\left(\frac{\overline{\kappa}_T}{\overline{\rho}}\right)\bigg|_o + \overline{h}\overline{\kappa}_{To}\frac{\mathrm{d}\overline{\kappa}_{Te}^2}{\mathrm{d}\overline{\rho}}\bigg|_o\right]\left(\frac{\mathrm{d}\overline{h}}{\mathrm{d}\theta}\right)^2\cos(\theta)\,\mathrm{d}\overline{\theta} \\ & + 8\pi^3 \int_0^{2\pi} \overline{\kappa}_{To}\overline{\kappa}_{Teo}^2\overline{h}^3\frac{\mathrm{d}^2\overline{h}}{\mathrm{d}\theta^2}\cos(\theta)\,\mathrm{d}\theta \\ & - 8\pi^3\frac{\mathrm{d}^2\overline{h}}{\mathrm{d}\theta^2}(0)\int_0^{2\pi}\overline{\kappa}_{To}\cos(\theta)\,\mathrm{d}\theta. \end{aligned} \tag{3.14}$$

We note that $\overline{\kappa}_T > 0$ for all fluids due to the Gibbs stability condition and both $\mathrm{d}\overline{h}/\mathrm{d}\theta$ and $\sin(\theta)$ are antisymmetric with respect to $\theta = \pi$. Thus, the quantity I_{x1} will always be non-zero. From conditions (2.5) we can also show that $I_{x1} < 0$ for all fluids. That is, the lowest order $\overline{F}_{x'} > 0$ so that the x'-component of the dimensional force on the rotor will point to the left in figure 2. On the other hand, the quantity $I_{x2} = 0$, because each term in the integrand of I_{x2} is symmetric with respect to $\theta = \pi$ except for $\mathrm{d}\overline{h}/\mathrm{d}\theta$ which is antisymmetric. In (3.14) the integrand of each integral is symmetric about $\theta = \pi$. As a result, each term of I_{x3} is seen to be non-zero.

If we substitute (3.1)–(3.4), (3.10) in (3.7), we then find

$$\frac{\pi\Lambda}{3}\overline{F}_{y'} = I_{y1} + \frac{I_{y2}}{\Lambda} + O\left(\frac{1}{\Lambda^2}\right), \tag{3.15}$$

where

$$I_{y1} = -2\pi\int_0^{2\pi}\frac{\overline{\kappa}_{To}}{\overline{h}}\frac{\mathrm{d}\overline{h}}{\mathrm{d}\theta}\cos(\theta)\,\mathrm{d}\theta, \tag{3.16}$$

$$I_{y2} = -4\pi^2\int_0^{2\pi}\overline{\kappa}_{To}\overline{\kappa}_{Teo}\overline{h}\frac{\mathrm{d}\overline{h}}{\mathrm{d}\theta}\sin(\theta)\,\mathrm{d}\theta. \tag{3.17}$$

We note that $\overline{\kappa}_{To}$, $\overline{h}$, and $\cos(\theta)$ are symmetric about $\theta = \pi$ while the derivative $\mathrm{d}\overline{h}/\mathrm{d}\theta$ is antisymmetric. Hence $I_{y1} = 0$ for all fluids. In like manner, it is easily demonstrated that $I_{y2} \neq 0$ in general. If we further require that the conditions (2.5) hold, the y'-component of the dimensional force on the rotor will be positive in figure 2.

From (3.11)–(3.17) we can obtain the approximation for the magnitude of the scaled load

$$\Lambda|\overline{\boldsymbol{F}}| = \frac{3|I_{x1}|}{\pi}\left[1 + \frac{1}{\Lambda^2}\left(\frac{I_{x3}}{I_{x1}} + \frac{1}{2}\frac{I_{y2}^2}{I_{x1}^2}\right) + O\left(\frac{1}{\Lambda^3}\right)\right], \tag{3.18}$$

and the angle of the load, i.e. attitude angle

$$\varphi \equiv \tan^{-1}\left(\frac{\overline{F}_{y'}}{\overline{F}_{x'}}\right) \approx \pi - \frac{1}{\Lambda}\frac{I_{y2}}{I_{x1}} + O\left(\frac{1}{\Lambda^2}\right), \tag{3.19}$$

where we have used the expansion of the tangent function for $\varphi \approx \pi$ in (3.19). Given the conditions (2.5), it is easily verified that

$$\frac{\pi}{2} \leqslant \varphi \leqslant \pi. \tag{3.20}$$

In order to obtain the expression for the approximate loss, we substitute the derivative of u, as given by (A 9), and the exact solution (2.11) in (2.18) yielding

$$-\overline{P} = \int_0^1 \frac{\overline{\mu}}{\overline{h}}\,\mathrm{d}\overline{x} + \frac{3}{\Lambda}\left(1 - \frac{1}{\Lambda}\frac{\mathrm{d}\overline{\rho}}{\mathrm{d}\overline{x}}(0)\right)\int_0^1 \frac{\overline{\kappa}_T}{\overline{\rho}^2}\frac{\mathrm{d}\overline{\rho}}{\mathrm{d}\overline{x}}\,\mathrm{d}\overline{x} + \frac{3}{\Lambda^2}\int_0^1 \frac{\overline{\mu}\overline{\kappa}_{Te}^2}{\overline{\rho}^5}\left(\frac{\mathrm{d}\overline{\rho}}{\mathrm{d}\overline{x}}\right)^2 \mathrm{d}\overline{x} + \frac{3}{\Lambda^2}\int_0^1 \frac{\overline{\mu}\overline{\kappa}_{Te}^2}{\overline{\rho}^5}\left(\frac{\mathrm{d}\overline{\rho}}{\mathrm{d}\overline{x}}\right)^2 \left(\overline{\rho}^3\overline{h}^3 - 1\right)\mathrm{d}\overline{x}. \tag{3.21}$$

We note that the second integral is identically zero and the last integral is seen to be $O(\Lambda^{-3})$. As a result, the second-order approximation for loss is found to be

$$-\overline{P} = \int_0^1 \frac{\overline{\mu}}{\overline{h}}\,\mathrm{d}\overline{x} + \frac{3}{\Lambda^2}\int_0^1 \overline{\kappa}_{Teo}\overline{\kappa}_{To}\overline{h}\left(\frac{\mathrm{d}\overline{h}}{\mathrm{d}\overline{x}}\right)^2 \mathrm{d}\overline{x} + O\left(\frac{1}{\Lambda^3}\right). \tag{3.22}$$

In (3.22) the values of $\overline{\mu}$ in the first integral have been left as their exact values. However, to be consistent, the shear viscosity in (3.22) should be expanded in a Taylor series for $\overline{\rho} \approx 1/\overline{h}$ in a manner similar to that done for (3.9). Alternatively, to simplify the computations, we evaluate the viscosity in the first integral of (3.22) by substituting the $O(\Lambda^{-2})$ density expansion (3.1) in the viscosity model. Errors in this approach will be of the order of the terms already neglected.

In the ideal gas limit, i.e. $\kappa_T \longrightarrow p \longrightarrow \rho RT$ and $\mu \longrightarrow \mu(T_{ref})$, we can take $\overline{\kappa}_T = \overline{\rho}$ and $\overline{\mu} = 1$ so that all the integrals in (3.18), i.e. (3.12)–(3.14) and (3.16)–(3.17), and (3.22) can be integrated explicitly. As a result, the expression of the scaled load can be written as

$$\Lambda|\overline{\boldsymbol{F}}| = \frac{12\pi(1+\delta-\sqrt{1+2\delta})}{\delta\sqrt{1+2\delta}}\left[1 + \frac{2\pi^2}{\Lambda^2}(1+\delta)(\sqrt{1+2\delta}-2)\right] + O\left(\frac{1}{\Lambda^3}\right), \tag{3.23}$$

and the attitude angle (3.19) becomes

$$\varphi \approx \pi - \frac{2\pi\sqrt{1+2\delta}}{\Lambda} + O\left(\frac{1}{\Lambda^2}\right). \tag{3.24}$$

The expression for the scaled loss can also be written as

$$-\overline{P} = \frac{1}{\sqrt{1+2\delta}} + \frac{12\pi^2}{\Lambda^2}(1+\delta-\sqrt{1+2\delta}) + O\left(\frac{1}{\Lambda^3}\right). \tag{3.25}$$

Our lowest-order load and loss, i.e. the first terms of (3.23) and (3.25), the expression of the attitude angle and the fact that the first corrections for the load and loss are $O(\Lambda^{-2})$ are consistent with the ideal gas results by Gross *et al.* (1980). The work here indicates that this ordering of the large Λ expansion also holds for general fluids. Examination of (3.18), (3.19) and (3.22)–(3.25) reveals that the lowest-order approximation of the scaled load and loss and attitude angle are dependent on δ and Λ alone when the gas is ideal. However, for pressurized gases, the lowest-order scaled load also depends on the variation of the scaled bulk modulus $\overline{\kappa}_T$; the lowest-order scaled loss depends on the variation of the scaled shear viscosity $\overline{\mu}$; the attitude angle depends on the variation of both $\overline{\kappa}_T$ and $\overline{\mu}$ in addition to δ and Λ.

4. Numerical results

In this section, we compare the approximation for the scaled load (3.18), scaled loss (3.22) and the attitude angle (3.19) to their exact values based on the density variation obtained from the exact Reynolds equation (2.8). More specifically, the exact Reynolds equation (2.8) was solved through the use of a straightforward shooting method. Once the pressure distribution was determined by substituting the resulting density variation in the equation of state, the exact scaled load was then computed using (2.13)–(2.15). The exact scaled loss was calculated using (2.18). The exact attitude angle was computed by taking the ratio of (2.14) to (2.13).

As described in § 3, the viscosity in the first integral of (3.22) was evaluated using the second-order density and the reference temperature. In the remaining integrals of our approximation, i.e. (3.12)–(3.14) and (3.17), the bulk modulus (1.3) and shear viscosity were computed based on the lowest-order density and the reference temperature. Derivatives of the bulk modulus and viscosity seen in (3.14) were estimated numerically. All numerical integrations of (2.13)–(2.14), (2.18), (3.12) and (3.14), (3.17) and (3.22) were computed using Simpson's rule. Discretization errors were checked for all computations presented here. For example, the difference in $\overline{\rho}$ between 200 and 300 points distributed over the interval $0 \leqslant \bar{x} \leqslant 1$ was less than 0.006 %. The tolerance for the value of $\overline{\rho}(1)$ for the shooting method was set to be 10^{-8}.

For the purpose of illustration, we use the Redlich–Kwong–Soave equation of state and the polynomial curve fit for the ideal gas specific heat provided in Reid, Prausnitz & Poling (1987). The fluid was chosen to be carbon dioxide (CO_2). The physical properties of CO_2 were taken from Reid *et al.* (1987); the critical pressure and temperature of CO_2 are $p_c = 73.77$ bar and $T_c = 304\,^{\circ}$K, respectively. The acentric factor for CO_2 was given by Reid *et al.* (1987) to be 0.239. The viscosity model is that of Chung *et al.* (1984, 1988). Parameters required for the application of the model of Chung *et al.* (1984, 1988) were taken from Reid *et al.* (1987). We take the channel sketched in figure 3 to be given by $h_o/L = 1.989 \times 10^{-5}$. Unless stated otherwise, $\delta = 0.5$.

We first consider the effect of pressurization on the load. In figure 7 we have plotted the variation of the lowest-order scaled load, i.e. the first term in (3.18), with the reference specific volume for a range of reference temperatures. At $T_{ref} = 1.05T_c$ pressurization can increase the scaled load by 56 % over the scaled load attained at low pressure. The physical reason for this increase can be seen by an examination of figure 8, in which the variation of $\overline{\kappa}_T$ with $\bar{x}$ is plotted for various thermodynamic states. At the lowest pressure, i.e. for $V(0) = 10V_c$, $\overline{\kappa}_T$ is < 1 over much of the range of $\bar{x}$. As the pressure is increased, the variation of $\overline{\kappa}_T$ from 1 decreases. At $V(0) = 2V_c$ and $1V_c$, it is seen that the values of $\overline{\kappa}_T$ are approximately one. As a result, the scaled load will be larger than that at low pressure. The observation that $\overline{\kappa}_T$ does not decrease significantly at high pressures is due to the non-monotone variation of the bulk modulus. At higher temperatures, the variation of the bulk modulus is a monotonically decreasing function of the specific volume. As a result, $\overline{\kappa}_T < 1$ over most of the bearing resulting in an insignificant increase in the scaled load.

We note that the scaled load in figure 7 remains nearly constant as the reference specific volume is varied in the range $V(0) > 4\ V_c$. This observation suggests that the load scales with the reference bulk modulus $\kappa_T|_{ref}$. This fact becomes obvious if we multiply (3.18) by

$$\frac{\kappa_T|_{ref}}{p_c}, \tag{4.1}$$

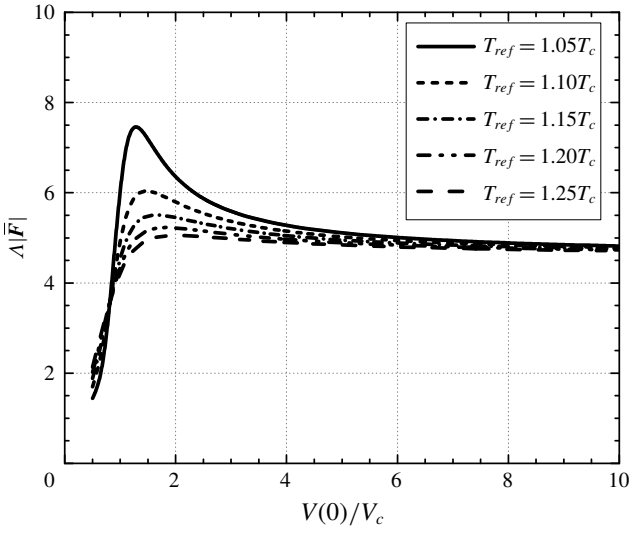

FIGURE 7. Lowest-order scaled load versus reference specific volume. The parameter $\delta = 0.5$.

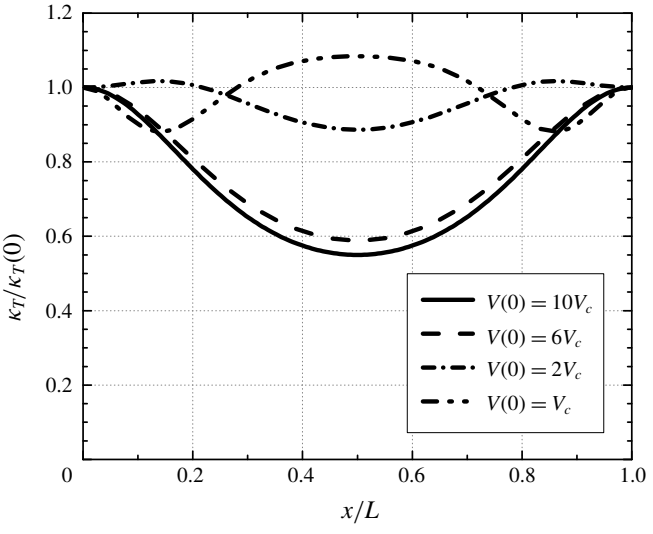

FIGURE 8. Scaled bulk modulus versus x/L for $T_{ref} = 1.05T_c$. The parameter $\delta = 0.5$.

and use (2.15). The resultant scaled load is

$$\frac{6|\boldsymbol{F}'|}{p_c R_i b}. \tag{4.2}$$

The scaled force (4.2) gives a measure of the physical force which is independent of the reference states. The variation of the lowest-order load (4.2) with reference thermodynamic state is plotted in figure 9. This version of the load is seen to increase significantly with pressurization at most temperatures and pressures. In the general

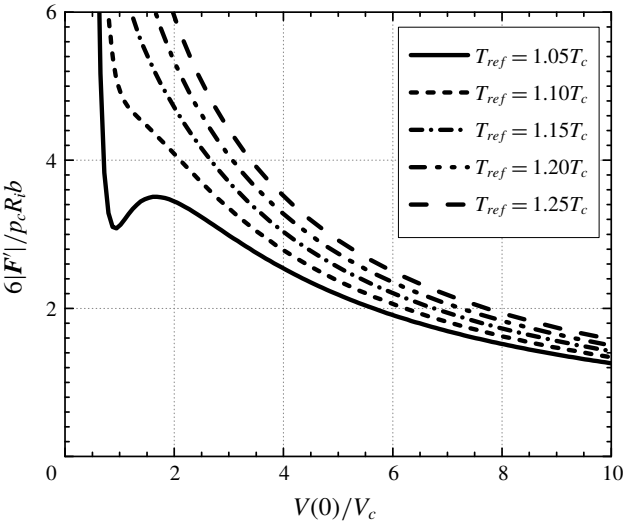

FIGURE 9. Rescaled load versus reference specific volume. The parameter $\delta = 0.5$.

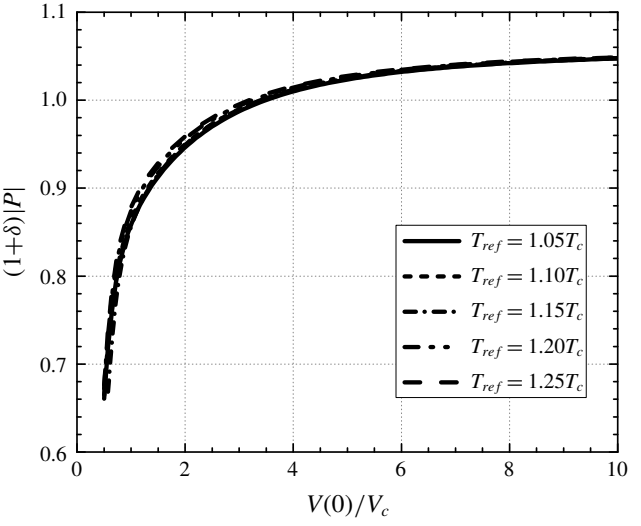

FIGURE 10. Lowest-order scaled loss versus reference specific volume. The parameter $\delta = 0.5$.

vicinity of the thermodynamic critical point, the non-monotone variation of the bulk modulus will give rise to a corresponding non-monotone variation in the load.

We next consider the lowest-order loss, i.e. the first term of (3.22), where $\overline{\mu}$ is evaluated at the lowest-order density. Following the conventional scaling used in the lubrication literature where the film thickness is scaled with the radial clearance, we have multiplied (3.22) by $1+\delta$ and have plotted this version of the scaled loss in figure 10 for various reference thermodynamic states. Inspection of figure 10 reveals that the reference temperature has an insignificant effect on the scaled loss. This is due to the fact that the shear viscosity roughly scales with the ideal gas shear viscosity,

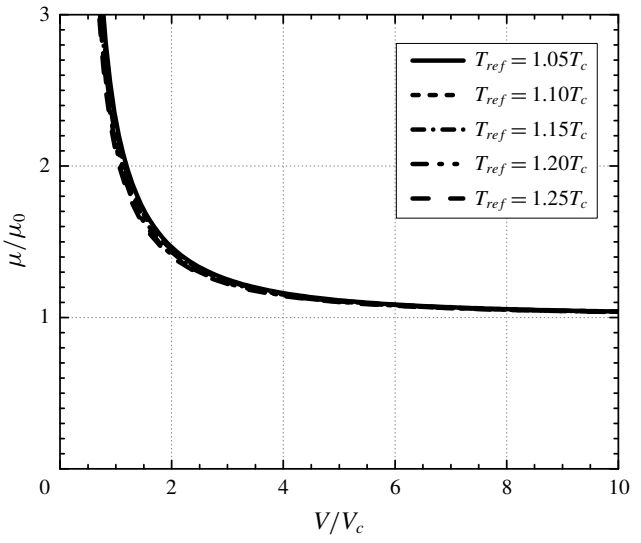

FIGURE 11. Scaled shear viscosity of CO_2 versus V/V_c. The viscosity model is that of Chung *et al.* (1984, 1988).

at least for the purposes of computing the temperature dependence. To illustrate this point, we have plotted the variation of the ratio of the shear viscosity to the ideal gas viscosity at the same temperatures in figure 11.

As indicated in the discussion of (3.25), the scaled loss for low-pressure gases will depend only on δ due to the fact that $\overline{\mu} = 1$ in the ideal gas limit. Thus, each curve in figure 10 will approach the same low-pressure asymptote for fixed δ. We note that the loss has been scaled with the loss found when the load is zero, i.e. when $\delta \equiv 0$. As a result, the scaled loss will always be larger than 1 as we approach the ideal gas limit. However, observation of figure 11 reveals that the viscosity will depend on the local density as the reference pressure is increased. Because the viscosity increases monotonically with increasing density, $\overline{\mu} < 1$ over most of the fluid domain. An example of the viscosity variation with $\bar{x}$ is plotted for various thermodynamic states in figure 12. As result, the scaled loss will decrease and even become less than 1 as the reference pressure is increased. That is, for pressurized gases the scaled loss generated by non-concentric cylinders can be smaller than that corresponding to concentric cylinders.

The effects of pressurization on the attitude angle are displayed in figure 13 for various reference temperatures at $\Lambda = 50$. Here we used the associated attitude angle $\psi \equiv \pi - \varphi$, i.e. the angle between the direction of the total force and the negative x' axis seen in figure 2. Inspection of figure 13 reveals that ψ increases with pressurization for a fixed reference temperature. At $T_{ref} = 1.05T_c$ pressurization results in 25.5 % increase of ψ over the value of ψ obtained at low pressure. The reason for this increase is due to the non-monotone variation of both $\overline{\kappa}_T$ and $\overline{\kappa}_{Te}$ leading to a smaller decrease in the size of the integrand in (3.17). At higher temperatures both $\overline{\kappa}_T$ and $\overline{\mu}$ monotonically increase as the pressure is increases. Thus, the integrands in (3.19) will be smaller and the increase in ψ will be smaller at higher temperatures.

A comparison of the approximate and the exact scaled load is plotted as a function of δ at $\Lambda = 20$, 30, 40, 50 and ∞ with various reference thermodynamic states in

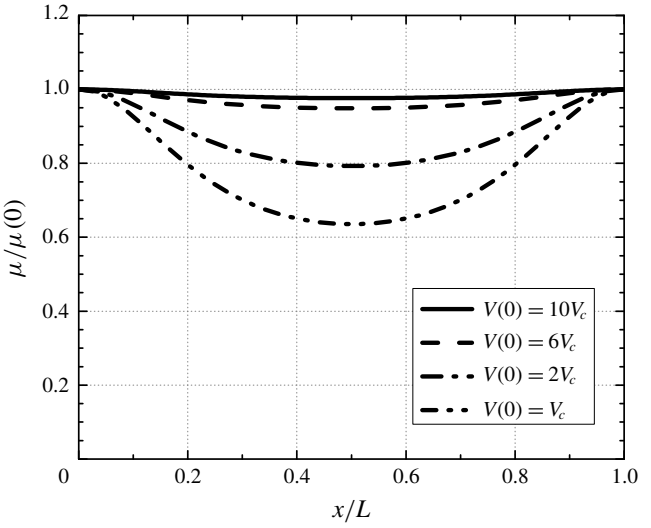

FIGURE 12. Variation of scaled viscosity with x/L for $T_{ref} = 1.05T_c$. The parameter $\delta = 0.5$.

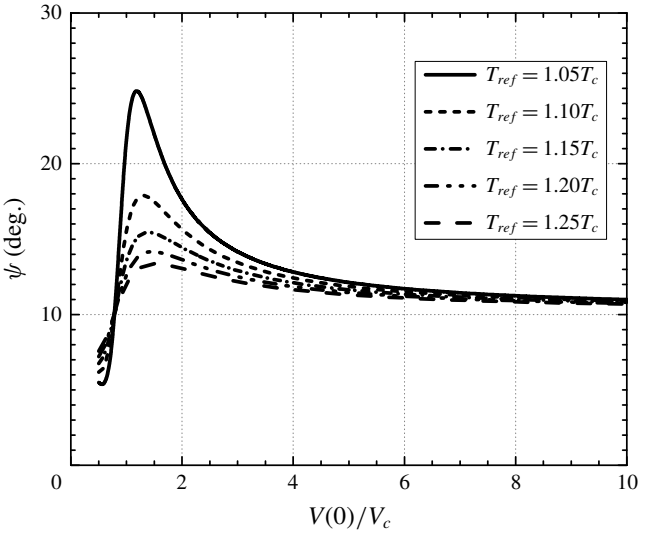

FIGURE 13. Attitude angle (ψ) versus reference specific volume. The parameter $\delta = 0.5$ and the speed number $\Lambda = 50$.

figure 14. The reference temperature is taken to be $T_{ref} = 1.15T_c$. The range of the speed numbers is selected to be within the general operating range described by previous investigators (Conboy 2013; Kim 2016). From (1.4) the rotational speeds corresponding to $\Lambda = 20$ at $V(0) = 12V_c$, $6V_c$ and $3V_c$ are found to be 8432 rpm, 14 221 rpm and 19 660 rpm, respectively. The solid lines denote the lowest-order theory and the broken lines represent the second-order approximation (3.18). At $V(0) = 12V_c$ there is little variation of the load with Λ and it is reasonable to suggest that the lowest-order approximation is sufficient to predict the scaled load for this

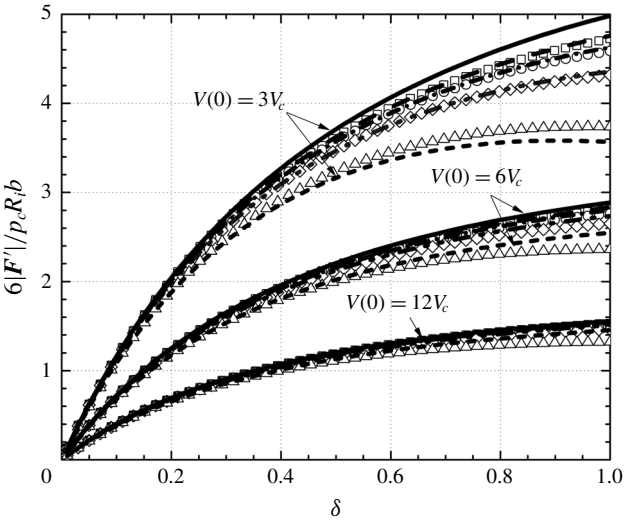

FIGURE 14. Scaled load versus δ at $V(0) = 3V_c$, $6V_c$ and $12V_c$. The speed numbers were taken to be $\Lambda = 20$, 30, 40, 50, ∞ and the reference temperature $T_{ref} = 1.15T_c$. Symbols represent the exact scaled load computed from (2.13)–(2.15) in which the pressure variation was obtained from the Reynolds equation (2.8) and the equation of state. Lines denote the approximation of the scaled load (3.18). The lowest-order results, i.e. $\Lambda = \infty$, are represented by ——. Results for $\Lambda = 50$ are denoted by □ and – – – –, results for $\Lambda = 40$ are denoted by ○ and – · – · –, results for $\Lambda = 30$ are denoted by ◇ and — · · — and results for $\Lambda = 20$ are denoted by △ and - - - -.

range of δ. As the reference pressure increases, the scaled load increases as expected, and more importantly, the effect of Λ on the scaled load is seen to become more significant. As a result, the second-order approximation is seen to be necessary to evaluate the load generated by pressurized gases. Even at $\Lambda = 20$ it was found that the maximum discrepancy between the second-order approximation and the exact scaled load for the case of $V(0) = 3V_c$ is 4.7 %.

In order to illustrate the effect of Λ on the loss, we have plotted the approximate and exact scaled loss as a function of δ at $V(0) = 12V_c$ and $3V_c$ in figure 15 and figure 16, respectively. The speed number $\Lambda = 20$, 30, 40, 50 and ∞, and the reference temperature was taken to be $T_{ref} = 1.15T_c$. Examination of figure 15 indicates that the agreement between the approximate and exact scaled loss is excellent for each Λ at $V(0) = 12V_c$. The maximum difference between the second-order approximation and the exact scaled loss is found to be 2.5 % at $\Lambda = 20$. The scaled loss is seen to decrease with the increase of Λ and to increase monotonically as δ increases. At higher pressures, the rate of increase of the viscosity with increasing density is larger than in the low-pressure case so that the loss for the case $V(0) = 3V_c$ has a local minimum located at $\delta \approx 0.2$. At these higher pressures the difference between the exact and approximate solutions is larger than in the low-pressure examples. Nevertheless, the maximum difference between the exact solution and the $\Lambda = 20$ approximation is less than 10 % for the chosen values of δ and $V(0)$.

The attitude angle ψ is plotted as a function of δ at $T_{ref} = 1.15T_c$ for $V(0) = 12V_c$ and $3V_c$ in figure 17 and figure 18, respectively. The speed numbers were taken to be $\Lambda = 20$, 30, 40 and 50. Observation of figure 17 reveals that the agreement between

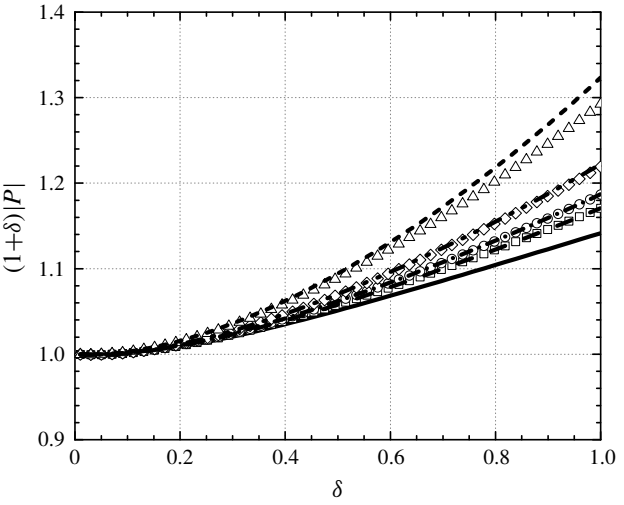

FIGURE 15. Scaled loss versus δ at $V(0) = 12V_c$. The speed numbers are taken to be $\Lambda = 20$, 30, 40, 50, ∞ and the reference temperature $T_{ref} = 1.15T_c$. Symbols represent the exact scaled loss computed from (2.18). Lines denote the approximation of the scaled loss (3.22). The lowest-order results, i.e. $\Lambda = \infty$, are represented by ——. Results for $\Lambda = 50$ are denoted by □ and – – – –, results for $\Lambda = 40$ are denoted by ○ and – – – –, results for $\Lambda = 30$ are denoted by ◇ and — · · — and results for $\Lambda = 20$ are denoted by △ and - - - -.

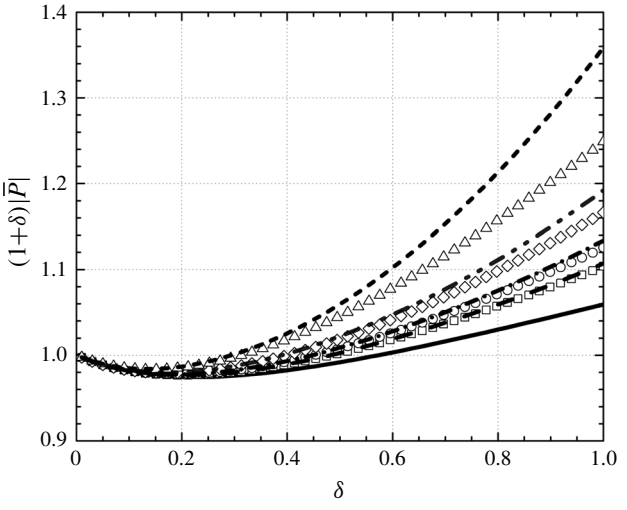

FIGURE 16. Scaled loss versus δ at $V(0) = 3V_c$. The speed numbers are taken to be $\Lambda = 20$, 30, 40, 50, ∞ and the reference temperature $T_{ref} = 1.15T_c$. Symbols represent the exact scaled loss computed from (2.18). Lines denote the approximation of the scaled loss (3.22). The lowest-order results, i.e. $\Lambda = \infty$, are represented by ——. Results for $\Lambda = 50$ are denoted by □ and – – – –, results for $\Lambda = 40$ are denoted by ○ and – · – · –, results for $\Lambda = 30$ are denoted by ◇ and — · · — and results for $\Lambda = 20$ are denoted by △ and - - - -.

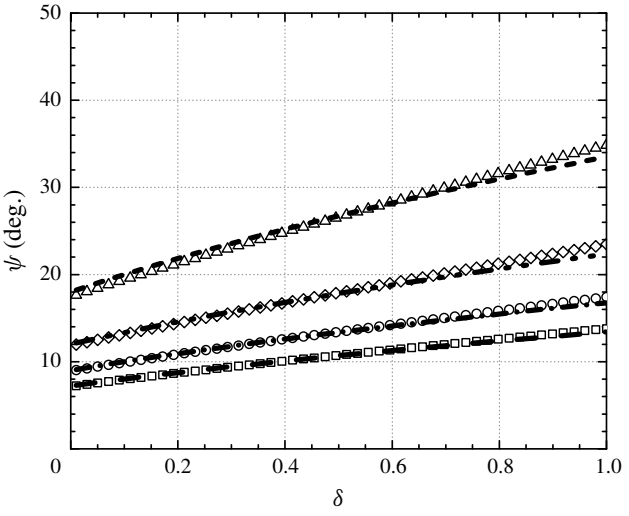

FIGURE 17. Attitude angle versus δ at $V(0) = 12V_c$. The speed numbers are taken to be $\Lambda = 20$, 30, 40 and 50 and the reference temperature $T_{ref} = 1.15T_c$. The scaled attitude angle is defined as $\psi \equiv \pi - \varphi$, i.e. the angle between the direction of the load and the negative x' axis seen in figure 2. Symbols represent the exact scaled attitude angle computed from (2.13) and (2.14). Lines denote the approximation of the scaled attitude angle obtained from (3.19). Results for $\Lambda = 50$ are denoted by □ and – – – –, results for $\Lambda = 40$ are denoted by ○ and — · —, results for $\Lambda = 30$ are denoted by ◇ and — · · — and results for $\Lambda = 20$ are denoted by △ and - - - -.

the exact ψ and the first-order approximate ψ is seen to be very good for each Λ at $V(0) = 12V_c$ where the maximum discrepancy is found to be 4 % at $\Lambda = 20$. The scaled attitude angle decreases with the increase of Λ and the decrease in δ. At $V(0) = 3V_c$, the first-order approximation of ψ still has reasonable agreement with the exact ψ when $\Lambda > 30$. At $\Lambda = 20$, the maximum difference between the exact ψ and approximate ψ is found to be 10.6 %. We note that the non-zero attitude angle at $\delta = 0$ is due to the fact that both $\overline{F}_{x'}$ and $\overline{F}_{y'} \longrightarrow 0$ at the same rate as $\delta \longrightarrow 0$. The limiting value of ψ can be found by taking $\delta \longrightarrow 0$ in (3.19), (3.12) and (3.17) yielding

$$\psi \sim \frac{2\pi}{\Lambda} \quad \text{as } \delta \longrightarrow 0. \tag{4.3}$$

Thus, ψ at $\delta = 0$ will be independent of the reference thermodynamic state. For $\Lambda =$ 20, 30, 40 and 50, the values of ψ at $\delta = 0$ will be 18°, 12°, 9° and 7.2°, respectively. This non-zero limit of ψ as δ vanishes is consistent with the finding of Gross *et al.* (1980) for ideal gases.

5. Summary

We have obtained approximate solutions for the load and loss of a two-dimensional, steady, compressible, laminar and single-phase flow between two non-concentric cylinders. Solutions are based on large Λ expansions of the Reynolds equation (2.8) and are therefore valid at most pressures and temperatures in the single-phase regime and for all Navier–Stokes fluids; the primary exception is the neighbourhood of the

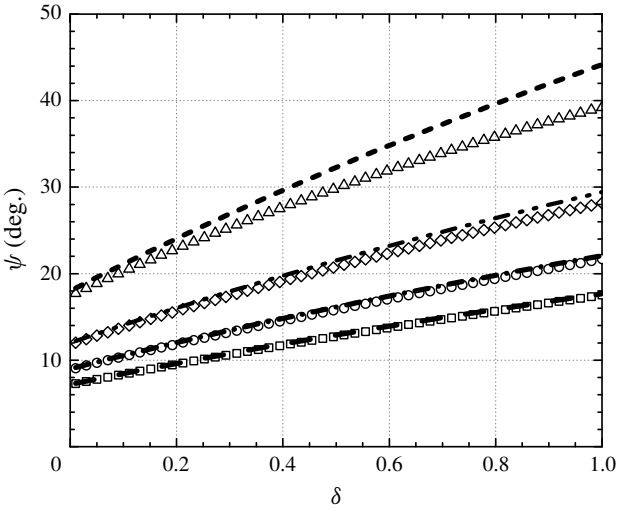

FIGURE 18. Attitude angle versus δ at $V(0) = 3V_c$. The speed numbers $\Lambda = 20$, 30, 40 and 50 and the reference temperature $T_{ref} = 1.15T_c$. The scaled attitude angle is defined as $\psi \equiv \pi - \varphi$, i.e. the angle between the direction of the load and the negative x′ axis seen in figure 2. Symbols represent the exact scaled attitude angle computed from (2.13) and (2.14). Lines denote the approximation of the scaled attitude angle obtained from (3.19). Results for $\Lambda = 50$ are denoted by □ and – – – –, results for $\Lambda = 40$ are denoted by ○ and — · —, results for $\Lambda = 30$ are denoted by ◇ and — · · — and results for $\Lambda = 20$ are denoted by △ and - - - -.

thermodynamic critical point where (2.8) breaks down. In appendix A we have given the connection between the friction loss and the net heat flux so that the heat transfer is determined once the friction loss is.

In the limit of ideal gases, the work of Gross *et al.* (1980) suggests that the first corrections to the load and loss are $O(\Lambda^{-2})$. The present study demonstrates that this ordering holds for general fluids, i.e. for both low- and high-pressure gases, as well.

The effects of pressurization and non-ideal gas behaviour have been illustrated primarily through the use of the lowest-order theory. Pressurization affects the load through the bulk modulus and it affects the loss through the density dependence of the shear viscosity. We found that the load scales with the reference bulk modulus $\kappa_T|_{ref}$ so that the non-monotone variations of the bulk modulus can result in a non-monotone variation of the load. Isothermal pressurization is seen to result in significant increases in the load.

At moderate pressures, inspection of figures 7 and 10 suggests that $\Lambda|\overline{\boldsymbol{F}}|$ and $(1+\delta)$ $|\overline{P}|$ can be regarded as nearly constant for reference specific volumes of $V(0) > 6V_c$. At higher pressures, the dependence of the density on the bulk modulus and viscosity becomes more noticeable. As a result, the strong decrease in the loss and the increase in the load will require the use of pure numerical solutions or the approximations given here.

The second-order approximations for load and loss are compared to the exact values obtained based on the solutions to the Reynolds equation (2.8) for a range of δ in figures 14–16. These examples illustrate the dependence of the load and loss on the eccentricity parameter (2.2) and the speed number.

The lowest-order attitude angle ($\psi \equiv \pi - \varphi$) has been computed and is found to decrease with increasing Λ. At constant Λ and a fixed reference thermodynamic state, the attitude angle is seen to approximately increase linearly with δ, at least for the cases shown. The values of ψ at $\delta = 0$ are given by (4.3) and are seen to be independent of thermodynamic state.

In order to focus on the physical effects of pressurization and the structure of the approximation scheme, we have restricted attention to the relatively simple flow model of Chien *et al.* (2017*a*); this model has been validated against numerical solutions to the full Navier–Stokes solutions in Chien *et al.* (2017*a*,*b*). Many of the observed features here are due to the density dependence of the material functions and will be present, to greater or lesser degrees, in more complex flows, including those involving turbulent and three-dimensional flows.

Appendix A. Relation of loss to heat transfer

In this appendix, we derive the relation between the heat transfer at the solid surfaces located at $y = 0$ and $y = h(x)$ in figure 3. The result is exact in the context of the approximations leading to (2.8). Chien *et al.* (2017*a*) have shown that the energy equation corresponding to (2.8) can be written

$$\frac{\partial \overline{q}_y}{\partial \overline{y}} = PrEc\left[\overline{\mu}\left(\frac{\partial u}{\partial \overline{y}}\right)^2 + (\beta T - 1)u\frac{\mathrm{d}\overline{p}}{\mathrm{d}\overline{x}} + u\frac{\mathrm{d}\overline{p}}{\mathrm{d}\overline{x}}\right], \tag{A 1}$$

where

$$\overline{q}_y \equiv -\overline{k}\frac{\partial \overline{T}}{\partial \overline{y}}, \tag{A 2}$$

is the scaled version of the y-component of the heat flux q_y and

$$\overline{k} \equiv \frac{k}{k_{ref}}, \tag{A 3}$$

$$Pr \equiv \frac{\mu_{ref} c_p|_{ref}}{k_{ref}}, \tag{A 4}$$

$$Ec \equiv \frac{U^2}{c_p|_{ref}\Delta T} \tag{A 5}$$

are the scaled thermal conductivity $k(\rho, T_{ref}) > 0$, Prandtl number and Eckert number. The quantity

$$\beta = \beta(\rho, T) \equiv -\frac{1}{\rho}\frac{\partial \rho}{\partial T}\bigg|_p \tag{A 6}$$

is the thermal expansivity and $c_p|_{ref}$ is the specific heat at constant pressure evaluated at the reference state. As discussed by Chien *et al.* (2017*a*), ΔT is determined by the flow details yielding $Pr\,Ec = 1$ when one of the walls is adiabatic.

Because the flow is isothermal to lowest order and $\overline{\rho} \approx \overline{\rho}(\overline{x})$ only, the variables $\overline{\mu}$, βT and $\mathrm{d}\overline{p}/\mathrm{d}\overline{x}$ can be regarded as independent of $\overline{y}$. The only $\overline{y}$ dependence will arise from the scaled velocity $u = v_x/U$, where v_x is the x-component of the particle velocity. This scaled velocity component satisfies the approximate momentum equation

$$\frac{\mathrm{d}\overline{p}}{\mathrm{d}\overline{x}} \approx \frac{\partial}{\partial \overline{y}}\left(\overline{\mu}\frac{\partial u}{\partial \overline{y}}\right). \tag{A 7}$$

By combining (A 7) with (A 1) and noting that $u=1$ at $\bar{y}=0$ and $u=0$ at $\bar{y}=\bar{h}$ we obtain the integral

$$\bar{q}_y|_{\bar{y}=\bar{h}} - \bar{q}_y|_{\bar{y}=0} + PrEc\left(\bar{\mu}\frac{\partial u}{\partial \bar{y}}\right)\bigg|_{\bar{y}=0} = PrEc(\beta T - 1)\frac{\mathrm{d}\bar{p}}{\mathrm{d}\bar{x}}\int_0^{\bar{h}} u\,\mathrm{d}\bar{y}. \tag{A 8}$$

To evaluate the last integral of (A 8) we use the solution to (A 7) subject to the no-slip conditions $u=1$ at $\bar{y}=0$ and $u=0$ at $\bar{y}=\bar{h}$ which can be written

$$u = 1 - (1 + A\bar{h}^2)\frac{\bar{y}}{\bar{h}} + A\bar{h}^2\frac{\bar{y}^2}{\bar{h}^2}, \tag{A 9}$$

where

$$A \equiv \frac{1}{2\bar{\mu}}\frac{\mathrm{d}\bar{p}}{\mathrm{d}\bar{x}} = \frac{3}{\Lambda}\frac{\bar{\kappa}_{Te}}{\bar{\rho}}\frac{\mathrm{d}\bar{\rho}}{\mathrm{d}\bar{x}}. \tag{A 10}$$

Substitution of (A 9) and (A 10), integration and straightforward manipulation yields

$$\bar{q}_y|_{\bar{y}=\bar{h}} - \bar{q}_y|_{\bar{y}=0} + PrEc\left(\bar{\mu}\frac{\partial u}{\partial \bar{y}}\right)\bigg|_{\bar{y}=0} = PrEc(\beta T - 1)\frac{\bar{\mu}A}{\bar{\rho}}\left[\bar{h}\bar{\rho} - \frac{\bar{h}^3\bar{\kappa}_{Te}}{\Lambda}\frac{\mathrm{d}\bar{\rho}}{\mathrm{d}\bar{x}}\right]. \tag{A 11}$$

Use of (2.11) yields

$$\bar{q}_y|_{\bar{y}=\bar{h}} - \bar{q}_y|_{\bar{y}=0} + PrEc\left(\bar{\mu}\frac{\partial u}{\partial \bar{y}}\right)\bigg|_{\bar{y}=0} = PrEc(\beta T - 1)\frac{\bar{\mu}A}{\bar{\rho}}\left[1 - \frac{1}{\Lambda}\frac{\mathrm{d}\bar{\rho}}{\mathrm{d}\bar{x}}(0)\right]. \tag{A 12}$$

We now integrate with respect to $\bar{x}$ from 0 to 1 and reuse (A 10) to obtain

$$\int_0^1 [\bar{q}_y|_{\bar{y}=\bar{h}} - \bar{q}_y|_{\bar{y}=0}]\,\mathrm{d}\bar{x} + PrEc\bar{P} = \frac{3PrEc}{\Lambda}\left[1 - \frac{1}{\Lambda}\frac{\mathrm{d}\bar{\rho}}{\mathrm{d}\bar{x}}(0)\right]\int_0^1 \frac{\bar{\kappa}_T}{\bar{\rho}^2}\frac{\mathrm{d}\bar{\rho}}{\mathrm{d}\bar{x}}\,\mathrm{d}\bar{x}, \tag{A 13}$$

where the definition (2.18) has been used. Because $\bar{\kappa}_T$ seen in the integral on the right-hand side is a function of $\bar{\rho}$ only and our periodicity conditions require that $\bar{\rho}(0)=\bar{\rho}(1)=1$, the fundamental theorem of calculus requires that the integral is zero yielding

$$\bar{P} = \frac{1}{PrEc}\int_0^1 [\bar{q}_y|_{\bar{y}=0} - \bar{q}_y|_{\bar{y}=\bar{h}}]\,\mathrm{d}\bar{x}. \tag{A 14}$$

Result (A 14) gives a direct relation between the work done by fluid friction to the heat which must be transferred out of the channel. If friction results in a loss of mechanical energy, $\bar{P} < 0$ and the net flow of heat energy will be out of the channel. We also note that the net heat transfer out of the fluid can be obtained once the loss is computed either numerically or the approximations derived in the § 3.

Chien & Cramer (2019) have shown that the variation of the thermal expansion coefficient (A 6) and therefore the flow work play an important role in the variation of the local heat fluxes. However, it should be clear from (A 14) that the net heat transfer is unaffected by the value of βT and therefore the flow work. The physical reason behind this observation is that the flow work is a reversible contribution. Therefore its net effect is zero when the total energy transfer is computed. The heat transfer is due solely to the irreversible work done by the viscous dissipation.

REFERENCES

BELL, I. H., WRONSKI, J., QUOILIN, S. & LEMORT, V. 2014 Pure and pseudo-pure fluid thermophysical property evaluation and the open-source thermophysical property library CoolProp. *Ind. Engng Chem. Res.* **53** (6), 2498–2508.

BRIGGS, M. H., PRAHL, J. M., BRUCKNER, R. & DYKAS, B. 2008 High pressure performance of foil journal bearings in various gases. In *STLE/ASME 2008 International Joint Tribology Conference*, pp. 403–405. American Society of Mechanical Engineers.

CHIEN, S. Y. & CRAMER, M. S. 2019 Pressure, temperature, and heat flux in high speed lubrication flows of pressurized gases. *Tribol. Intl* **129**, 468–475.

CHIEN, S. Y., CRAMER, M. S. & UNTAROIU, A. 2017*a* Compressible Reynolds equation for high-pressure gases. *Phys. Fluids* **29** (11), 116101.

CHIEN, S. Y., CRAMER, M. S. & UNTAROIU, A. 2017*b* A compressible thermohydrodynamic analysis of journal bearings lubricated with supercritical CO_2. In *ASME Conference Paper FEDSM2017-69310*.

CHUNG, T. H., AJLAN, M., LEE, L. L. & STARLING, K. E. 1988 Generalized multiparameter correlation for nonpolar and polar fluid transport properties. *Ind. Engng Chem. Res.* **27** (4), 671–679.

CHUNG, T. H., LEE, L. L. & STARLING, K. E. 1984 Applications of kinetic gas theories and multiparameter correlation for prediction of dilute gas viscosity and thermal conductivity. *Ind. Engng Chem. Fundam.* **23** (1), 8–13.

CONBOY, T. M. 2013 Real-gas effects in foil thrust bearings operating in the turbulent regime. *J. Tribol.* **135** (3), 031703.

CONBOY, T. M., WRIGHT, S. A., PASCH, J., FLEMING, D., ROCHAU, G. & FULLER, R. 2012 Performance characteristics of an operating supercritical CO_2 Brayton cycle. *Trans. ASME J. Engng Gas Turbines Power* **134** (11), 111703.

CRESPI, F., GAVAGNIN, G., SÁNCHEZ, D. & MARTÍNEZ, G. S. 2017 Supercritical carbon dioxide cycles for power generation: a review. *Appl. Energy* **195**, 152–183.

DELLACORTE, C., RADIL, K. C., BRUCKNER, R. J. & HOWARD, S. A. 2008 Design, fabrication, and performance of open source generation I and II compliant hydrodynamic gas foil bearings. *Tribol. Trans.* **51** (3), 254–264.

DOSTAL, V., DRISCOLL, M. J. & HEJZLAR, P. 2004 A supercritical carbon dioxide cycle for next generation nuclear reactors. *Tech. Rep.* MIT-ANP-TR-100.

DOUSTI, S. & ALLAIRE, P. 2016 A compressible hydrodynamic analysis of journal bearings lubricated with supercritical carbon dioxide. In *Proceeding of Supercritical CO_2 Power Cycle Symposium. San Antonio, TX*.

GROSS, W. A., MATSCH, L. A., CASTELLI, V., ESHEL, A., VOHR, J. H. & WILDMANN, M. 1980 *Fluid Film Lubrication*. Wiley.

GUENAT, E. & SCHIFFMANN, J. 2018 Real-gas effects on aerodynamic bearings. *Tribol. Intl* **120**, 358–368.

HAMROCK, B. J., SCHMIDT, S. R. & JACOBSON, B. O. 2004 *Fundamentals of Fluid Film Lubrication*. CRC Press.

HESHMAT, H., WALTON, J. F. & CORDOVA, J. L. 2018 Technology readiness of 5th and 6th generation compliant foil bearing for 10 MWE s-CO_2 turbomachinery systems. In *Proceeding of the 6th International Supercritical CO_2 Power Cycles Symposium. Pittsburg, PA*.

HOWARD, S. A., BRUCKNER, R. J., DELLACORTE, C. & RADIL, K. C. 2007 Gas foil bearing technology advancements for closed Brayton cycle turbines. In *AIP Conference Proceedings*, vol. 880, pp. 668–680. AIP.

KIM, D. 2016 Design space of foil bearings for closed-loop supercritical CO_2 power cycles based on three-dimensional thermohydrodynamic analyses. *J. Engng Gas Turbines Power* **138** (3), 032504.

LEMMON, E. W., HUBER, M. L. & MCLINDEN, M. O. 2002 NIST Reference fluid thermodynamic and transport properties – REFPROP. *NIST Standard Reference Database* **23**, v7.

PENG, Z. C. & KHONSARI, M. M. 2004 On the limiting load-carrying capacity of foil bearings. *J. Tribol.* **126** (4), 817–818.

PINKUS, O. & STERNLICHT, B. 1961 *Theory of Hydrodynamic Lubrication*. McGraw-Hill.

QIN, K. 2017, Development and application of multiphysics simulation tools for foil thrust bearings operating with carbon dioxide. PhD thesis, University of Queensland.

REID, R. C., PRAUSNITZ, J. M. & POLING, B. E. 1987 *The Properties of Gases and Liquids*. McGraw-Hill.

REYNOLDS, O. 1886 On the theory of lubrication and its application to Mr. Beauchamp Tower's experiments, including an experimental determination of the viscosity of olive oil. *Proc. R. Soc. Lond.* **40** (242–245), 191–203.

SZERI, A. Z. 2010 *Fluid Film Lubrication*. Cambridge University Press.

WRIGHT, S. A., RADEL, R. F., VERNON, M. E., ROBERT, G. E. & PICKARD, P. S. 2010 Operation and analysis of a supercritical CO_2 Brayton cycle. *Sandia Report*, No. SAND2010-0171.